The Cryosphere

Optical properties of sea ice doped with black carbon – an experimental and radiative-transfer modelling comparison

Amelia A. Marks, Maxim L. Lamare, and Martin D. King

Department of Earth Sciences, Royal Holloway University of London, Egham, Surrey, TW20 0EX, UK

Correspondence: Martin D. King (m.king@rhul.ac.uk)

Abstract. Radiative-transfer calculations of the light reflectivity and extinction coefficient in laboratory-generated sea ice doped with and without black carbon demonstrate that the radiative-transfer model TUV-snow can be used to predict the light reflectance and extinction coefficient as a function of wavelength. The sea ice is representative of first-year sea ice containing typical amounts of black carbon and other light-absorbing impurities. The experiments give confidence in the application of the model to predict albedo of other sea ice fabrics.

Sea ices, ~ 30 cm thick, were generated in the Royal Holloway Sea Ice Simulator (~ 2000 L tanks) with scattering cross sections measured between 0.012 and 0.032 $m^2 kg^{-1}$ for four ices. Sea ices were generated with and without ~ 5 cm upper layers containing particulate black carbon. Nadir reflectances between 0.60 and 0.78 were measured along with extinction coefficients of 0.1 to 0.03 cm^{-1} (*e*-folding depths of 10–30 cm) at a wavelength of 500 nm. Values were measured between light wavelengths of 350 and 650 nm. The sea ices generated in the Royal Holloway Sea Ice Simulator were found to be representative of natural sea ices.

Particulate black carbon at mass ratios of ~ 75, ~ 150 and ~ 300 $ng g^{-1}$ in a 5 cm ice layer lowers the albedo to 97, 90 and 79 % of the reflectivity of an undoped "clean" sea ice (at a wavelength of 500 nm).

1   Introduction

Rapid decline of sea ice in the Arctic is often seen as a bellwether for modern day climate change (e.g. IPCC, 2013). Model predictions of future sea ice extent have a large de-gree of uncertainty (e.g. IPCC, 2013). Accurate representation and re-creation of the optical and physical properties of sea ice is essential to develop accurate models of sea ice. The Royal Holloway (RHUL) Sea Ice Simulator facility aims to create a realistic sea ice within a controlled environment with the ability to monitor both the physical (temperature, salinity and density) and optical (nadir reflectivity and extinction co-efficient) properties of the sea ice – the results of which can be used to evaluate sea ice models.

The following study presents the first data from the RHUL sea ice simulator used to validate the Tropospheric Ultraviolet–Visible (TUV)-snow radiative-transfer model for use with sea ice. The TUV-snow model is a coupled atmosphere–snow radiative-transfer model, described in detail by Lee-Taylor and Madronich (2002). The model has been used multiple times for investigations of radiative transfer in snow (e.g. King et al., 2005; France et al., 2011, 2012; Reay et al., 2012) and has also been adapted for use with sea ice (e.g. King et al., 2005; Marks and King, 2013, 2014; Lamare et al., 2016). The model has previously been experimentally validated for photochemistry in snow by Phillips and Simpson (2005), but it has not been experimentally validated for sea ice.

The TUV-snow model will first be evaluated by comparing measured optical properties (reflectance and extinction coefficient) of sea ice grown in a laboratory to TUV-snow model radiative-transfer calculations for a sea ice with the same properties. Second, the model will be evaluated by comparing measured nadir reflectance with light-absorbing impurities in the laboratory sea ice to radiative-transfer calculations with the same light-absorbing impurities in the sea ice, namely black carbon and algae.

Sea ice typically contains impurities such as black carbon, sediment and algae (e.g. Perovich, 1996). Black carbon is an efficient absorber of solar radiation (e.g. Mitchell, 1957; Highwood and Kinnersley, 2006; Hansen and Nazarenko, 2004; Jacobson, 2001; Ramanathan and Carmichael, 2008; Bond et al., 2013) and its deposition onto, or incorporation into, sea ice has been shown through modelling calculations to decrease the surface reflectance of the sea ice, increasing melt rates (e.g. Grenfell et al., 2002; Jacobson, 2004; Light et al., 1998; Ledley and Thompson, 1986; Goldenson et al., 2012; Holland et al., 2012; Marks and King, 2013, 2014). To evaluate the TUV-snow model with black carbon, a commercial black carbon is added to a 5 cm surface layer of 30–50 cm thick sea ice created in the laboratory in mass ratios of 0, 75, 150 and 300 ng g^{-1} and the nadir reflectance of sea ice measured. The experimental reflectivity is compared to a calculated reflectivity using the TUV-snow model, for the same black carbon mass ratios. The work presented here will demonstrate that radiative-transfer modelling with TUV-snow model (Lee-Taylor and Madronich, 2002) can reproduce laboratory-grown ices with differing fabrics with a range of mass ratios of light-absorbing impurities. Such a validation will give confidence to others in the calculations of TUV-snow for other sea ice types and other light-absorbing impurities.

Previous research on the effects of black carbon on sea ice optical properties have used radiative-transfer calculations and global climate model simulations. To the authors' knowledge there are no laboratory or field studies examining the effects of added black carbon on reducing sea ice reflectance. A related study by Hadley and Kirchstetter (2012) carried out successful laboratory experiments on artificial snow, investigating the effects of black carbon on snow reflectance. The results from Hadley and Kirchstetter (2012) were used to validate the Snow, Ice and Aerosol radiation (SNICAR) model L (Flanner et al., 2007) used in the 2013 IPCC report (IPCC, 2013). Similarly, Brandt et al. (2011) investigated the effect of black carbon on albedo of artificial snowpacks using snowmaking machines, showing a good match between measured values and albedos calculated from radiative-transfer modelling. Peltoniemi et al. (2015) measured the effect on snow bidirectional reflectance owing to additions of chimney soot, volcanic sand and glaciogenic silt, demonstrating how snow metamorphism caused by the addition of these particles subsequently impacted on the albedo.

The study presented here includes the first experiments with the Royal Holloway Sea Ice Simulator, the first experiments to evaluate the TUV-snow radiative-transfer model for calculations of extinction coefficient and reflectivity of undoped sea ice, the first experimental results to demonstrate the change in reflectance owing to light-absorbing impurities in sea ice and finally the first experiments to evaluate the accuracy of the TUV-snow model for reflectivity calculations for light-absorbing impurities in sea ice.

Throughout the paper the term "experimental" refers to experiments with laboratory-grown sea ice using the sea ice simulator described in Sect. 2.1, with results being referred to as "measured" values. The term "modelled" refers to calculations from the TUV-snow radiative-transfer model, the results of which are referred to as "calculated" values.

2 Experimental method

The following sections will describe the design of the sea ice simulator (Sect. 2.1), the characterization of both the optical and physical properties of the laboratory ice (Sect. 2.2) and the creation of sea ice doped with black carbon particles (Sect. 2.3).

2.1 Sea ice simulator design

The sea ice simulator is designed to replicate a Polar sea ice growth environment under UV and visible wavelengths of solar radiation. Previous experiments with sea ice simulators have been carried out by, for example, Light et al. (2015), Buist et al. (2011), Papadimitriou et al. (2003), Haas et al. (1999), Polach et al. (2013), Hare et al. (2013) and Grenfell and Perovich (1981). The setup of the simulator is shown in Fig. 1. The simulator is housed in a refrigerated shipping container (11.95 m length × 2.56 m height × 2.29 m width), which can be temperature controlled from −25 to 25 °C. The air temperature within the container varies by ±1 °C – although thermocouples monitoring temperature at the ice surface show better temperature stability, and the temperature variation measured within the ice is less than the precision of the probes (±0.2 °C). Every 12 h the chiller removes ice build-up on the cooling plant and air temperature rises briefly by ∼ 6 °C. Inside the container, sea ice is formed in a 2000 L polyethylene cylindrical white plastic tank (1.32 m height × 1.39 m diameter) placed on insulated pallets. Following the approach of Perovich and Grenfell (1981), a cylindrical design is utilized for the tank to help avoid mechanical stress at particular locations. A 1 cm insulating layer of black neoprene also surrounds the tank sides. A metal Unistrut frame surrounds the tank to further improve structural integrity. Black wooden boards, painted with mould resistant paint, are fixed around the Unistrut structure with 3 cm thick polystyrene insulation fitting between the wooden boards and the tank.

The tank is filled with a solution of Tropic Marin (Atkinson and Bingman, 1997) giving water with a salinity of 32 PSU, representing Arctic Ocean salinity (Boyer et al., 2013). Tropic Marin is a synthetic sea salt mixture for aquaculture containing over 70 chemical elements in typical natural concentrations representative of the ocean with the notable exception of nitrate and phosphate, to inhibit algae growth. Atkinson and Bingman (1997) show that the concentrations of major cations and anions of Tropic Marin are
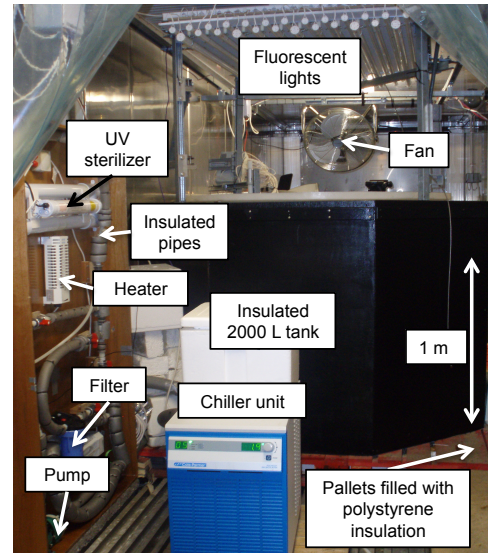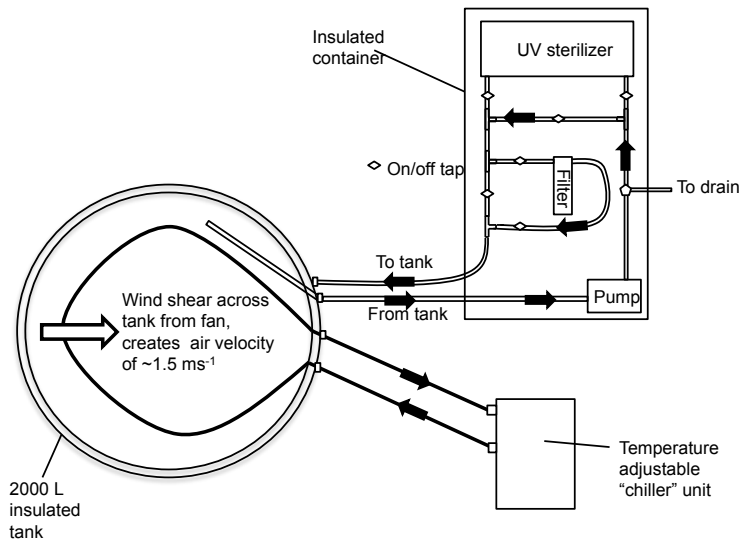
Figure 1. Plan of the sea ice simulator showing the 2000 L cylindrical tank (1.32 m height × 1.39 m diameter) in plan view and water conditioning unit in horizontal view and annotated photo of the facility. A closed pipe runs around the base of the tank connected to a heater unit circulating a water and glycol mixture gently warming the base of the tank. Water is circulated around the tank by a pump in an insulated container and also passed through a UV sterilizer and particulate filter. Note that the diffusing hood and insulation have been stripped away for clarity in the photo.

within 10 % of seawater. Previous sea ice simulators use either sodium chloride or synthetic sea salt mixtures similar to Tropic Marin (e.g. Krembs et al., 2001; Mock et al., 2002; Papadimitriou et al., 2003; Hare et al., 2013).

To create circulation within the tank, ensuring temperature and salinity stratification does not occur, an Iwaki MD-10 pump circulates water at $\sim 10\,\mathrm{L\,min^{-1}}$ at the base of the tank, as shown in Fig. 1. The circulated water is also pumped through a 10 μm filter to remove any particulate impurities and a UV sterilizer to prevent algae growth.

Sea ice grows from surface cooling of a salt water body (Weeks, 2010). To ensure even and realistic ice growth in the tank (from the surface, downwards) a closed pipe is run around the bottom of the tank, connected to a heater unit. The heater unit contains a solution of water and pure ethylene glycol (in a 1 : 1 ratio), which is pumped around the pipe at a constant temperature (0 °C), to warm the base of the tank and prevent freezing. Figure 2 demonstrates that the temperature of the water beneath the sea ice is not thermally stratified; ice temperature decreases linearly through the ice with depth and the ice surface temperature is at a constant −15 °C.

Illumination, during optical measurements only, and replicating shortwave solar wavelengths over 350–650 nm, is provided with a set of 20 Daystar daylight simulation fluorescent tubes and five sun-bed ultraviolet tube lights (peak illumination wavelength ~ 350, 40 nm FWHM). Measurement of reflectance of the sea ice is a relative measurement, (i.e. the quotient of reflected radiance of sea ice to reflected radiance from a reflectance standard); thus, the intensity spectrum of the lamp does not have to match the solar spectrum.
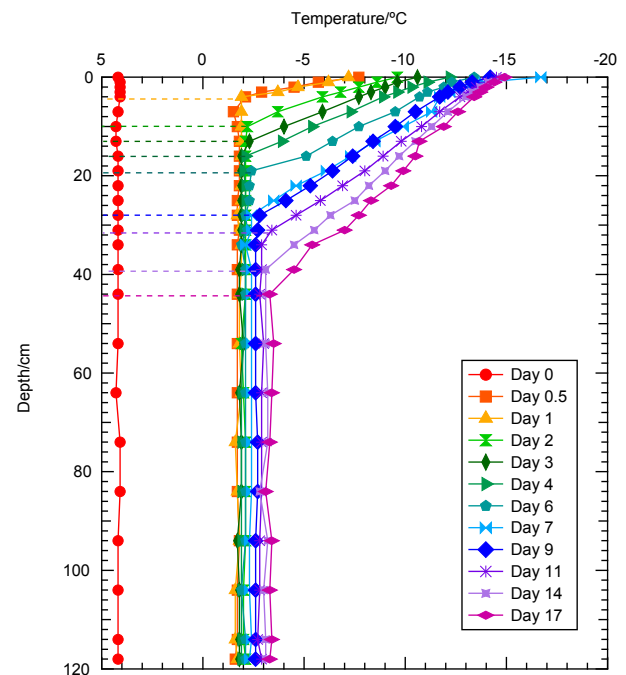

Figure 2. Temperature profiles through ice during ice growth. The top section, showing a linear increase in temperature, represents measurements from the ice, while the bottom section, with a constant temperature, shows measurements from the under-ice seawater, demonstrating that the water is not thermally stratified.
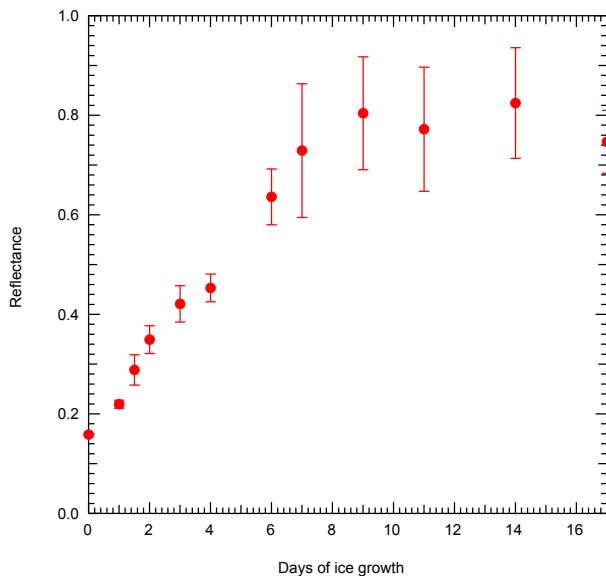
Figure 3. Reflectance of sea ice during ice growth and the day-to-day reflectance stability of the potentially optically thick ice (day 10 onwards).

The lights are evenly distributed directly above the tank to provide a diffuse illumination source. The light is further diffused by opaque white boards placed around the edges of the tank. Diffuse lighting was used to simplify the measurement of extinction coefficient and provide a useful reflectance product. The radiance, as a function of azimuth and zenith angle, within the experiment was checked with a fibre optic probe and a broadband visible wavelength measurement and was found to vary by 5–10 %. The short term variability of the lamps was less than 0.1 % (after an initial warm-up) on the timescale of the measurement of reflectivity or e-folding depth. Note that both the value of nadir reflectance (relative to a Spectralon panel) and light penetration depth are not dependent on the illumination irradiance, providing the irradiance does not change during the measurement. Figure 3 shows the change in ice nadir reflectance during ice growth and the day-to-day reflectance stability of the optically thick ice.

2.2　Creation and characterization of sea ice

To create sea ice, an air temperature inside the container of $\sim -15\,°C$ is maintained. Cold air is circulated within the container with fans. An additional air fan, attached to the ceiling, blows cold, ambient air at the water surface ($110\,m^3\,min^{-1}$), increasing the heat flux from the ice surface, quickening ice formation and assisting the production of columnar ice (Weeks, 2010).

Sea ice is grown in the simulator for ~ 17 days, producing ice with a thickness of $\sim 30\,cm$. Temperature–depth profiles and nadir reflectance of the ice were measured daily during

growth (described in Sect. 2.2.1 and 2.2.3 respectively). The extinction coefficient is measured at the end of the experiment as it destroys the homogeneity of the ice (described in Sect. 2.2.4).

Characterization of sea ice physical properties

2.2.1　Temperature profiles

Temperature profiles through the sea ice are recorded daily during ice growth to give an indication of sea ice thickness and ensure that temperature stratification does not occur within the underlying seawater. The temperature is recorded via a series of thermocouples, as used by Rabus and Echelmeyer (2002), Johnston and Timco (2002) and Nomurai et al. (2006). Calibrated type T thermocouples are each inserted into a thin plastic sleeve and then a white polypropylene pole at regular depths (every 2 cm) into the water, and then frozen in place during ice formation. The precision of all the thermocouples at $-15\,°C$ was measured as $\pm 0.2\,°C$. Temperature of sea ice decreases from the surface to the base; ice thickness can be determined from the point where the temperature becomes constant with depth – which can be assumed to be seawater, as shown in Fig. 2.

2.2.2　Determining sea ice properties by ice coring

Cores of the ice are taken to determine sea ice properties at the conclusion of the optical experiments (Sect. 2.2). The corer design was based on a CRREL report by Rand and Mellor (1985). Cores are photographed, divided into $\sim 5\,cm$ sections and their dimensions and mass measured to derive density. Salinity is measured after melting using a Fisher Scientific seawater refractometer (cross-calibrated with an accurate ion conduction probe).

Characterization of sea ice optical properties

2.2.3　Measuring reflectance

The nadir reflectance of the sea ice was measured daily during ice growth until the value became constant (taking between 6 and 12 days). Reflectance becomes constant once a sufficient ice thickness is reached such that the increasing ice thickness does not change the measured reflectivity. Upwelling radiance from the ice is measured via an optical lens connected to a $400\,\mu m$ XSR fibre optic coupled to an Ocean Optics USB 2000+ spectrometer (wavelength range: 200–850 nm; resolution: 1.5 nm FWHM; signal : noise 250 : 1). The optical lens is situated $\sim 40\,cm$ above the sea ice surface at nadir with a view footprint covering a circular area $\sim 315\,cm^2$. The footprint is an order of magnitude larger than any surface feature on the sea ice.

To convert ice surface radiance measurements to reflectance, the radiance of light from the sea ice surface measured at nadir is ratioed to the radiance from a reference Lam-

bertian reflector at nadir (a Spectralon panel) measured in the same location but raised 5 mm above the ice surface and under identical illumination as the sea ice.

During a reflectivity measurement a 30 cm × 30 cm Spectralon panel is added to the diffuse lighting environment above the sea ice. The addition of this panel increases the radiance, L, within the diffuse lighting environment. A very conservative estimate of the effect on the measurement of the reflectivity can be calculated by analogy to an integrating sphere. The Spectralon panel represents 0.66 % of the area of the diffuse lighting environment, which is approximately a cube made up of white panels and sea ice (i.e. 6 m × 1.5 m × 1.5 m = 13.5 m^2). Treating the diffuse lighting environment above the sea ice as a crude integrating sphere and considering fractional change in radiance, $\frac{\delta L}{L}$, after Ball et al. (2013), who suggest $\frac{\delta L}{L} \approx \frac{A_{panel}}{A_{environment}\rho}$, where A_{panel} is the area of the Spectralon panel, $A_{environment}$ is the area of the diffusing "cube" and ρ is the overall reflectivity of the diffusing cube. A very crude analysis assumes that reflectivity of the panel is 1 and the part fraction of the hypothetical integrating sphere is 0. In the limit of a reflective environment, $\frac{\delta L}{L} \rightarrow \frac{A_{panel}}{A_{environment}\rho} \sim 0.67$ %. Thus the overestimation of the radiance (~ 0.67 %) is significantly less than the uncertainty displayed on the measurement of nadir reflectivity displayed in Figs. 3 and 7.

2.2.4 Measuring extinction coefficient

At the completion of the experiment the extinction coefficient and e-folding depth are measured. The e-folding depth is the distance over which light intensity reduces to $\frac{1}{e}$ of its initial value and is the reciprocal of the extinction coefficient. The e-folding depth is reported in addition to the extinction coefficient. The sea ice e-folding depth and extinction coefficient is measured by drilling a single hole gradually through the ice in ~ 5 cm increments with a sharp drill. At each depth drilled the same fibre optic is inserted into the hole and the light intensity (upwelling radiance) is measured via an Ocean Optics spectrometer. In an optically thick sea ice the measurement of either up or downwelling light for e-folding depth is not important, as has been shown by France and King (2012). The hole is a tight fit around the fibre, but a thin, light diffusing disc of white PTFE is also placed around the fibre at the ice surface, to minimize any stray light entering the hole without altering the light field near the hole.

Simultaneously to the light intensity in the hole being measured (I_{raw}), the light intensity of another fibre optic inside a diffusing PTFE container at the ice surface was measured (I_{ref}), to account for any change in the intensity of the fluorescent lights. The relative light intensity at depth z, namely I_z, is then calculated:

$$I_z = \frac{I_{raw(z)}}{I_{ref}}.$$ (1)

The e-folding depth, ϵ, is calculated using Eq. (2), where I_z is the relative intensity at a depth z, and $I_{z'}$ is intensity at the shallowest depth, z'. From the measured light intensity the e-folding depth is calculated by fitting an exponential curve through I_z versus z data:

$$\frac{I_z}{I_{z'}} = e^{-\left(\frac{(z-z')}{\epsilon}\right)}.$$ (2)

The extinction coefficient, k, is than calculated as the reciprocal of the e-folding depth.

Measurements used to calculate the e-folding depth are only conducted in the middle of the ice as the irradiance profile changes rapidly at the air–ice and ice–water boundary (a good example is shown in King et al., 2005). The calculation of an e-folding depth from the modelled downwelling irradiance was calculated from similar depths as the experimental ice. The modelled ice had the same thickness and underlying tank radiance field as the experiment. The extinction coefficient and e-folding depth measured in the work presented here are asymptotic (reaching a constant value as shown in King et al., 2005) as the light field to the sea ice is diffuse and thus there are no near-surface effects as found frequently in fieldwork (e.g. Reay et al., 2012, and references therein).

2.3 Creation of black-carbon-doped sea ice

Once the sea ice has grown to ~ 30 cm thick (~ 3 weeks of ice growth) 75 L (equivalent to a ~ 5 cm layer) of chilled seawater doped with a known concentration of black carbon (described in Sect. 2.3.1) is added to the surface and frozen in place forming a 5 cm black carbon bearing ice layer. Black carbon is placed within a 5 cm surface layer of the artificial ice to replicate black carbon entrainment into sea ice following melting of overlying snow as described by Grenfell et al. (2002) and Doherty et al. (2010). The new 5 cm layer of black carbon bearing seawater is left to freeze for 3 days and the reflectivity of the new sea ice surface then measured daily over a week. The sea ice is then cored and density and salinity measured down the core to record the physical ice structure before and after the black carbon bearing layer is added.

At completion of the experiment the ice is melted and water is purified by filtration through a 1 μm Purtex filter to remove black carbon particulates. If any black carbon particulates were to remain the concentration would be negligible, as it would be diluted by 2000 L of sea water (a dilution factor of ~ 30). The whole process is repeated with other black carbon concentrations in the 5 cm layer, giving a total of four mass loadings: ~ 75, ~ 150 and ~ 300 ng g^{-1} and a blank run with 0 ng g^{-1} of black carbon. The sea ice was melted and the resulting seawater was treated with aqueous hypochlorous acid (HOCl) and filtered between experimental runs to remove any algae that may have grown. No algae were visible to the naked eye.

2.3.1 Creating atmospherically representative black carbon

To create the aqueous black carbon solutions a method from Clarke (1982) is adapted. The black carbon used, Monarch 120, is produced by Cabot Corporation to replace the discontinued Monarch 71 used by Grenfell et al. (2011). Approximately 1 g of the black carbon is added to a solution of 800 mL of pure water and 200 mL isopropanol (isopropanol aids dispersal of the black carbon in the concentrated solution) (Clarke, 1982). The solution is then placed in an ultrasonic bath for 2 h to ensure that the black carbon is fully dispersed and to break up conglomerated lumps. The solution is then suction filtered through 2 μm Nuclepore membrane filters followed by 0.8 μm Nuclepore filter to remove larger particles and ensure the final solution is representative of atmospheric black carbon, i.e. particle diameter < 0.8 μm (Clarke, 1982). The mass loading of black carbon in the solution is determined gravimetrically (i.e. by evaporating and weighing a portion of the black carbon solution). Two black carbon solutions were used, with mass loadings of 46 ± 11 and 11 ± 1.5 μg g^{-1}. The uncertainties are the standard deviation of three repeated gravimetric determinations. Known amounts of solutions 1 and 2 are mixed with 75 L of artificial seawater to give overall black carbon mass ratios detailed in Table 1. The mass ratios of black carbon are approximately 0, 75, 150 and 300 ng g^{-1}; these approximate values will be subsequently used in the text, whilst precise values are reported in Table 1.

2.3.2 Characterization of black carbon optical properties

The mass absorption cross section of the black carbon used in the present study is estimated using an integrating sandwich spectrometer, described by Grenfell et al. (2011), based on Clarke (1982). The integrating sandwich spectrometer measures the absorption spectrum of particulate matter on filter samples in a diffuse radiance environment. Absorption spectra of multiple filters containing black carbon loadings are converted to a mass absorption cross section. A mass absorption cross section of 2.1 m^2 g^{-1} ($\lambda = 610$ nm) is estimated for the black carbon placed in the artificial sea ice. The values are a factor of 3 smaller than the black carbon mass absorption cross section of 6.57 m^2 g^{-1}, for a wavelength of 610 nm (Flanner et al., 2007), typically used in radiative-transfer calculations, but are similar to values used by Dang et al. (2015) owing to the size of the black carbon particles used.

Six known aliquots of the filtered black carbon solution described in Sect. 2.3.1 were filtered through 0.4 μm Nuclepore filters, providing filter loadings of 10.18, 15.12, 20.15, 25.19, 50.38 and 100.77 μg cm^{-2}. The absorbance spectra of the filters (Fig. 4a) are calculated using

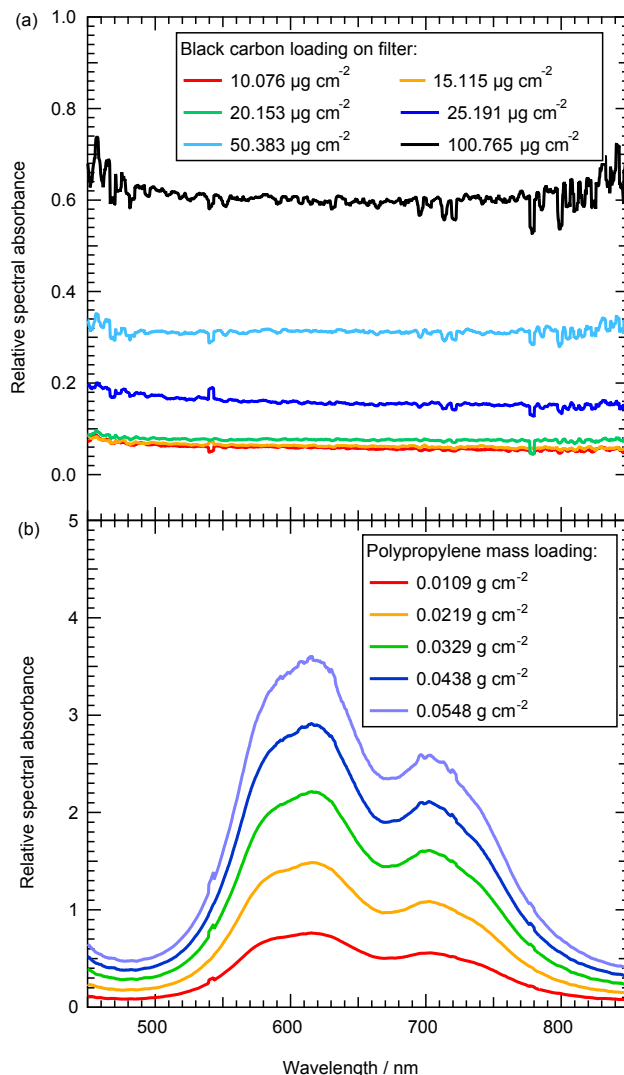$$A(\lambda) = -\ln \frac{I(\lambda)}{I_0(\lambda)}, \qquad (3)$$

Figure 4. (a) Relative spectral absorbance of black carbon versus wavelength for various loadings of black carbon on the filter. **(b)** Relative spectral absorbance versus wavelength for different mass loadings of polypropylene.

where I is the intensity measured with the loaded filter in the integrating sandwich spectrometer, and I_0 is the intensity measured with a blank 0.4 μm Nuclepore filter, which is measured following the same procedure as the loaded filter. To calibrate the integrating sandwich spectrometer, a set of translucent standard plastic sheets (light blue polypropylene, 100 μm) with measurable mass absorption coefficients are used. The sheets are placed on a 0.4 μm Nuclepore filter and measured in the integrating sandwich spectrometer using the same method as the black carbon filters. Multiple sheets of the polypropylene are stacked, providing loadings of 0.011, 0.0219, 0.0329, 0.0439 and 0.0548 g cm^{-2} (Fig. 4b) Grenfell et al. (2011) showed that for small amounts of black carbon the mass loading is directly proportional to

Table 1. Optical and physical properties of sea ice for each run, including the mass ratio of black carbon added to the top layer of ice, density of ice and scattering cross section (σ_{scatt}) of both the top and bottom layers of the ice. The uncertainty in sea ice density is 1 standard deviation of the average of measurements taken from the core profile. Uncertainty is not provided for the density of the top layer as this is the average of only two measurements, although the uncertainty is likely to be similar to that of the lower layer. The mass ratio of black carbon added to the surface layer is also shown. The uncertainty in the black carbon mass ratio is the uncertainty in the gravimetric method used for determining the mass ratio, as described in Sect. 2.3.1.

Run number	Black carbon mass ratio added/ng g^{-1}	Density of bottom (undoped) layer/g cm^{-3}	Density of top (doped) layer/g cm^{-3}	σ_{scatt} bottom layer/m^2 kg^{-1}	σ_{scatt} top BC layer/m^2 kg^{-1}
1	0	0.91 ± 0.084	0.92	0.315 ± 0.040	0.05
2	77 ± 18	0.91 ± 0.059	0.91	0.235 ± 0.041	0.05
3	153 ± 37	0.92 ± 0.044	1.00	0.115 ± 0.004	0.35
4	305 ± 62	0.95 ± 0.050	0.93	0.126 ± 0.016	0.2

the absorbance measured by the integrating sandwich spectrometer. In this study, we considered the linear sensitivity between the black carbon mass loading and the black carbon absorbance with the ratio between black carbon and polypropylene and we equate the ratio of sensitivities to the ratio of the mass absorption cross section. Therefore, the mass absorption cross section of the black carbon is expressed as

$$\sigma_{\text{BC}} = \sigma_{\rho l} \frac{\alpha_{\rho l}}{\beta_{\text{bc}}}, \qquad (4)$$

where $\alpha_{\rho l}$ is the slope of the linear regression between the mass loading of the polypropylene calibration sheets and the relative absorbance of the polypropylene measured in the integrating sandwich spectrometer, β_{bc} is the slope of the linear regression between the mass loading of the black carbon filters and the relative absorbance of the black carbon measured in the integrating sandwich spectrometer and $\sigma_{\rho l}$ is the mass absorption cross section of the polypropylene, given by the Beer–Lambert law.

The mass absorption coefficients of the polypropylene sheets are measured with a standard spectrometer using the Beer–Lambert law. The measured mass absorption coefficient is 229.23 ± 0.02 cm^2 g^{-1} ($\lambda = 610$ nm).

To visually investigate the size and shape of the black carbon particles used in the experiment, scanning electron microscopy (SEM) is employed. Approximately 6 mm wide squares of the 0.4 µm filters containing black carbon particles were cut and glued on standard 12.7 mm diameter SEM stubs using double-faced carbon tabs. The samples were gold coated using a Polaron E5100 Series II Cool Sputter Coater for 3 min in air, creating a 45 nm thick coating. SEM images were generated on a Hitachi S3000N scanning electron microscope. The images were obtained at a magnification of $\times 4000$ at a working distance of 12.5 mm, with an acceleration energy of 20 kV and a beam current of 85 000 nA. Figure 5 shows a SEM image of black carbon particles on a 0.4 µm Nuclepore filter. The SEM images are analysed using the ImageJ image analysis software (Abramoff et al., 2004),

to determine the size distribution and the circularity of the black carbon particles. The circularity of the particles is determined by the shape factor (Heilbronner and Barrett, 2013), calculated using

$$\text{SF} = \frac{4\pi A}{P^2}, \qquad (5)$$

where A is the area of the shape and P the perimeter of the shape. The shape factor represents the deviation of the perimeter of a particle from a circle of the same area. Values of the shape factor vary between 0, representing an elongated shape, and 1, describing a circle. The average shape factor of the particles shown in Fig. 5 is 0.842, indicating a rough spherical shape. Assuming a spherical nature of the particles, the diameter is calculated as the maximum Feret diameter. The average diameter of the particles shown in Fig. 5 is 0.461 ± 0.331 (2σ) µm.

The mass absorption coefficients of the black carbon is also estimated by a Mie light scattering calculation using the SEM data. Mie calculations are performed using size data from the SEM to provide a check of the value for black carbon absorption cross section for the radiative-transfer calculations. For the Mie calculations the black carbon diameter of 0.461 µm is used with a density of 1.8 g cm^{-3} and a commonly used refractive index of $1.8–0.5i$ (Clarke and Noone, 1985), giving an absorption cross section at a wavelength of 550 nm of 2.78 m^2 g^{-1}.

In the work presented here an absorption cross section value of 2.5 m^2 g^{-1} will be used for radiative-transfer calculations, as this is between the value from the Mie calculations and that from the integrating sandwich spectrometer.

3 TUV-snow radiative-transfer calculations

Calculations using the TUV-snow radiative-transfer model (described in Sect. 3.1) are undertaken to simulate the optical and physical properties measured of the sea ice. For undoped ice, reflectance and extinction coefficient/e-folding depth are
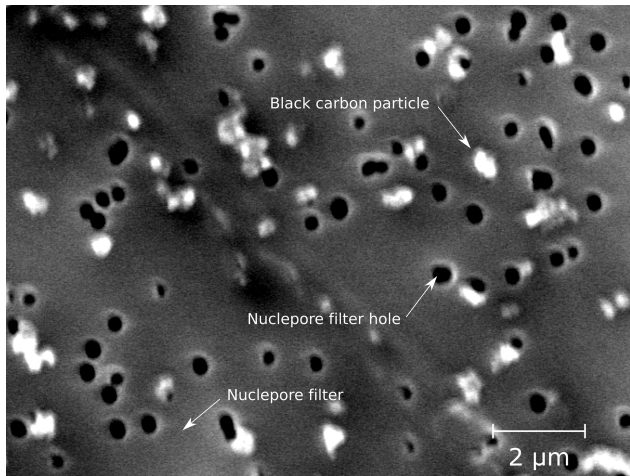
Figure 5. Scanning electron microscope image of gold coated black carbon particles (white) at a magnification of ×4000, showing a roughly spherical shape of the particles and an average particle diameter of $0.461 \pm 0.331\,\mu m$. Note that the image also shows the Nuclepore filter holes at $0.4\,\mu m$ diameter.

calculated (Sect. 3.2), while for sea ice with black carbon the model is used to calculate only reflectance (Sect. 3.3).

3.1 The TUV-snow radiative-transfer model

The TUV-snow model is a coupled atmosphere–snow–sea-ice radiative-transfer model using the DISORT code (Stamnes et al., 1988) and is described in detail by Lee-Taylor and Madronich (2002). The model parameterizes sea ice optical properties using only an asymmetry factor, g, a wavelength-independent scattering cross section, σ_{scatt}, a wavelength-dependant absorption cross section, σ_{abs}^{+}, and sea ice density and thickness.

3.2 Calculations of undoped ice reflectance and extinction coefficient/e-folding depth

The reflectance and extinction coefficient/e-folding depth of the undoped sea ice are calculated through radiative-transfer calculations using the TUV-snow model with derived scattering and absorption cross sections for the ice. To derive these values, values of scattering and absorption cross section are varied until they reproduce the experimentally measured reflectivity and e-folding depth data for the sea ice as detailed in King et al. (2005), France et al. (2011, 2012) and Marks and King (2014). Ice density and thickness are measured from ice cored at the end of an experiment. The density of the ice is detailed in Table 1. The ice is modelled with a 30 cm thick bottom layer subdivided into 45 sub-layers with each sub-layer representing 1 cm apart from the bottom and top five sub-layers which are 1 mm thick. The asymmetry factor for the ice is fixed at 0.95, based on a value suggested

by Mobley et al. (1998) for a bubble-rich ice, which is observed in ice cores taken from the tank.

All calculations are undertaken between wavelengths 350 and 650 nm, using eight-streams in DISORT. The wavelength-dependant nadir reflectance of the water-filled tank is measured and included in the model as the under-ice reflectance; the measurements are included in the Supplement. The model illuminates the ice with diffuse light.

Reflectivity is calculated as the ratio of upwelling, Irr_{up}, to downwelling Irr_{down}, irradiance at the surface of the sea ice, $\left(\frac{Irr_{up}}{Irr_{down}}\right)$. The e-folding depth is calculated using Eq. (2), and the irradiances are calculated at depths of 5, 10, 15 and 20 cm in the sea ice with reference irradiance at a depth of 5 cm (to reproduce experimentally derived e-folding depths). The extinction coefficient is calculated as the reciprocal of the e-folding depth.

3.3 Calculating surface reflectance of ice with a black-carbon-doped layer

The radiative-transfer modelling was repeated for the black-carbon-doped sea ices. For these radiative-transfer calculations, parameters are kept the same as the undoped ice calculations, although the ice is modelled as two layers; a 30 cm thick undoped bottom layer and a 5 cm upper, black carbon bearing, layer. These principal layers are subdivided into 45 sub-layers for the bottom layer and 14 sub-layers in the top layer, with each sub-layer being 1 cm thick, apart from 0.5 cm either side of a boundary (air–ice, undoped ice–doped ice and ice–water), where sub-layers are 1 mm.

The absorption cross section of the top layer was the same as the bottom undoped layer plus additional absorption for any black carbon present (0, 75, 150 and 300 ng g^{-1}), where the absorption cross section of the black carbon is $2.5\,m^2\,g^{-1}$ (see Sect. 2.3.2). The scattering cross section of the top layer was derived by a trial and error method to obtain the best fit (judged by eye) between modelled and measured values of reflectance and e-folding depth as described in Sect. 4.3. Densities of the top layers are shown in Table 1.

4 Results

4.1 Physical properties of sea ice and growth rates

Salinity, density and temperature–depth profiles of all ice cores are given in the Supplement. A typical salinity and temperature profile is given in Fig. 6. The average density for the top and bottom layer for each black carbon loading is shown in Table 1.

Ice growth rates were similar for all runs with the ice growing at approximately 1.8 cm per day. For all runs the growth rate gradually declined as ice growth progressed. The time taken for reflectance of the ice to become a constant value became longer, taking 5 days for run 1, 7 days for run 2, 11 days
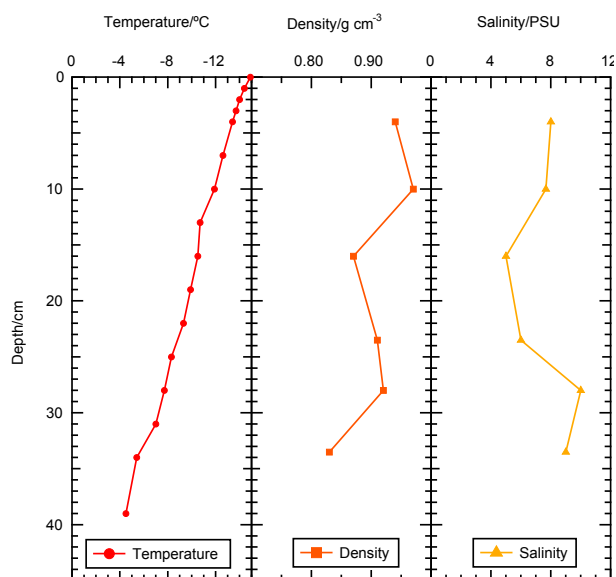
Figure 6. Example temperature, salinity and density data for an ice core from run 2 before the black carbon bearing layer was added.

Figure 7. Measured sea ice surface reflectance versus wavelength (solid shapes) and modelled sea ice reflectance versus wavelength (dashed lines) for sea ice with no added black carbon.

for run 3 and 13 days for run 4, owing to an issue with the maintenance of the refrigerator plant which reduced its heat flux from the simulator but not its maintained temperature. The sea ice produced for each run had a slightly different fabric and subsequently produced less scattering sea ice, as shown by the value of σ_{scatt} in Table 1.

4.2 Measured and modelled reflectivity and extinction coefficient/*e*-folding depth of undoped sea ice

4.2.1 Experimental measurements and calculations of reflectance and extinction coefficient/*e*-folding depth for undoped ice

The measured nadir reflectance of the undoped ice layer is shown in Fig. 7 for the four runs. Each run represents an experiment with new sea ice growth before the black carbon bearing layer is added. The reflectance is wavelength dependent, peaking at values around 500 nm, as would be expected for sea ice (e.g. Grenfell and Maykut, 1977). Measurements of reflectance shown in Fig. 7 are the average of 5 days of reflectance measurements taken when ice reflectance had become constant. The reflectance of the undoped sea ice decreases from run 1 to run 4, which is attributable to the slightly different ice fabrics in each run and the fact that the ice thickness is not optically thick.

The extinction coefficient and *e*-folding depth of the undoped ice, Fig. 8, are also wavelength dependent, with the largest values of *e*-folding depth observed around 550 nm for all runs, again representing a natural sea ice (e.g. Grenfell and Maykut, 1977). The *e*-folding depths increase with run number, which is again attributable to the different ice fab-
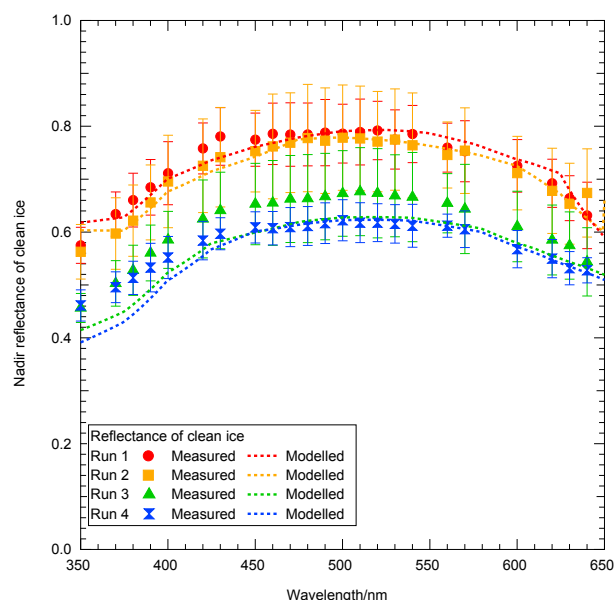
rics created. The increased *e*-folding depth can be attributed to a less light scattering sea ice matrix.

Figures 7 and 8 also contain the modelled reflectivity and extinction coefficient/*e*-folding depth fitted to the experimental data. With the exception of the UV nadir reflectivity of runs 3 and 4, the modelled fits are well within uncertainty of the measurement.

It should be noted that it is more difficult to find a pair of values for scattering and absorption cross sections (σ_{scatt} and σ_{abs}^{+}) for each wavelength that produce a good reproduction of the experimental reflectivity and *e*-folding depth, rather than reflectivity alone, as the system described here is significantly more constrained in the number of degrees of freedom. Thus, measuring reflectivity and *e*-folding depth gives the reader more confidence in the values of σ_{scatt} and σ_{abs}^{+}.

4.2.2 Derived absorption and scattering cross sections from experimental data for undoped ice

The calculated values of the absorption cross section of impurities in the undoped ice used in the radiative-transfer calculations are shown in Fig. 9. The shape of the derived absorption cross section for each run is similar, decreasing slightly with increased run number. Ideally, the absorption should be zero for undoped ice (no impurities). Absorption cross sections of Saharan dust from Lamare et al. (2016) and chlorophyll in algae from Bricaud et al. (2004) and Mundy et al. (2011) are shown in Fig. 9 for comparison to the sea ice impurity absorption cross section. A characteristic signal of chlorophyll in algae is present. It should be noted that the algae presence was unintentional, not observed by the naked
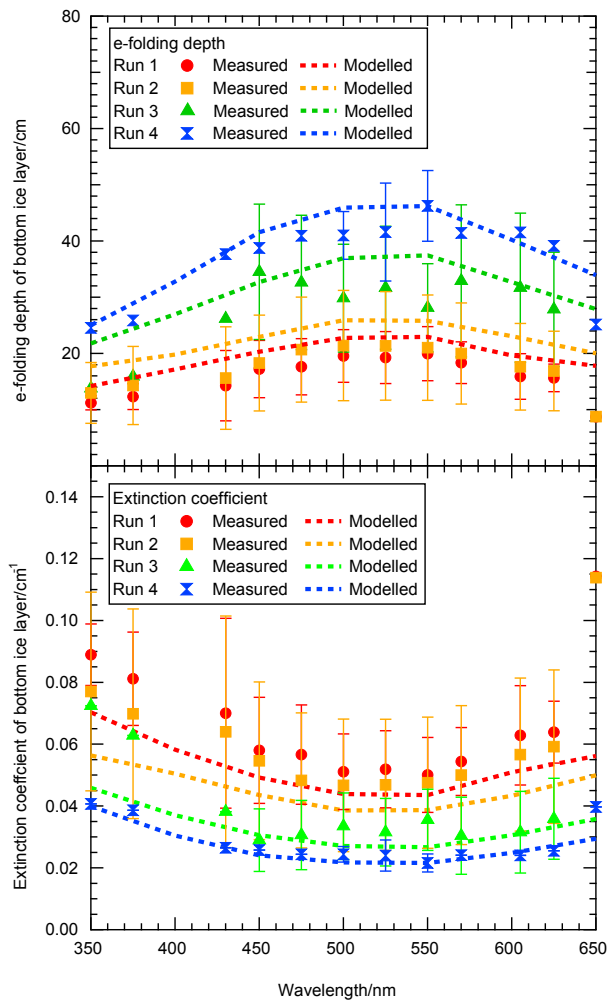
Figure 8. Top: measured sea ice *e*-folding depth versus wavelength (solid shapes) and modelled sea ice *e*-folding depth versus wavelength (dashed lines) for sea ice with no added black carbon. Bottom: measured sea ice extinction coefficient versus wavelength (solid shapes) and modelled sea ice extinction coefficient versus wavelength (dashed lines).

eye, and resisted several cycles of disinfection. It is testament to the sensitivity of the technique for deriving absorption and scattering cross sections that the absorption cross section of the algae can be calculated.

The modelled scattering coefficient used in the radiative-transfer calculations is wavelength independent and reported in Table 1.

4.3 Surface reflectivity of black-carbon-doped sea ice

The reflectance of the sea ice with an extra 5 cm black carbon bearing ice layer decreases at all wavelengths as the black carbon mass ratio increases, as shown in Fig. 10. At a wavelength of 500 nm, reflectance decreases to 97 % of the reflectance of undoped ice (Run 1) for an addition of seawater
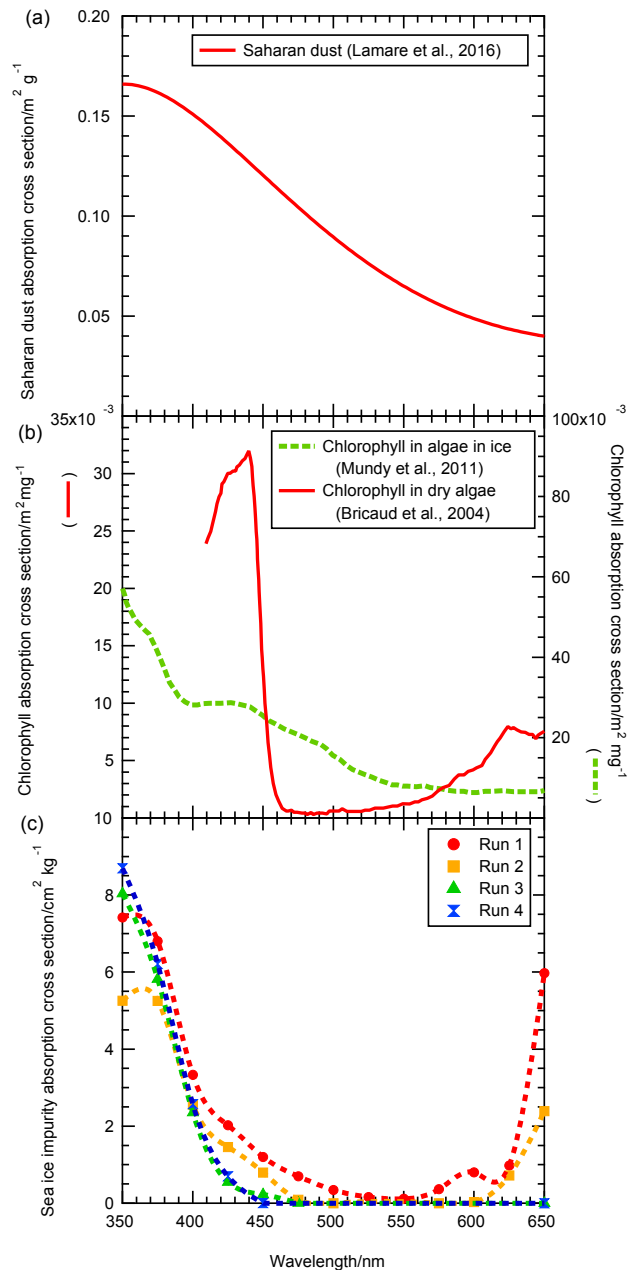

Figure 9. (a) Absorption cross section of Saharan dust taken from Lamare et al. (2016). **(b)** Absorption cross sections of chlorophyll. Chlorophyll in ice (dashed line) taken from Mundy et al. (2011) is per milligram of algae determined by fluorescence. Chlorophyll (solid line) is taken from Bricaud et al. (2004) and is per milligram of dry weight cells. **(c)** Wavelength-dependent absorption cross section derived from reflectance and *e*-folding depth data from runs 1 to 4 for the undoped ice. A smooth line is added to guide the eye. Values for run 4 are too small to plot clearly at longer wavelengths. Error bars show the possible variation in absorption cross section obtained from different fits of the original reflectance and *e*-folding depth data.
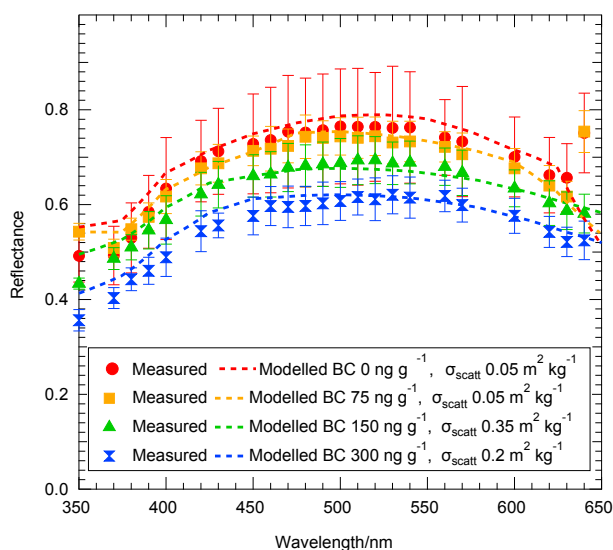
Figure 10. Comparison between measured (solid shapes) and calculated (dashed lines) reflectance of laboratory sea ice surface with black carbon in a 5 cm surface layer in varying mass ratios. The figure shows the best fit possible by altering scattering cross section of the upper black carbon bearing layer (values shown on plot).

with a mass ratio of black carbon of $75 \, \mathrm{ng \, g^{-1}}$, to 90 % for an addition with a mass ratio of $150 \, \mathrm{ng \, g^{-1}}$ compared to undoped ice and to 79 % for an addition with a mass ratio of $300 \, \mathrm{ng \, g^{-1}}$ compared to reflectivity of undoped ice.

The extinction coefficient/e-folding depth of the ice after the black carbon layer was added was not measured, as the total ice could no longer be considered a homogeneous medium and the 5 cm doped layer was too thin to measure the extinction coefficient in this layer alone.

The best fit obtained between the measured and calculated reflectance values from varying the scattering cross section of the upper sea ice layer between realistic values is shown in Fig. 10. These values of the scattering cross section are shown in Fig. 10, varying from 0.05 to $0.35 \, \mathrm{m^2 \, kg^{-1}}$. The fit between the measured and calculated reflectance is well within uncertainty limits for all runs, demonstrating that the TUV-snow model can reproduce experimental reflectance for sea ice doped with black carbon, even with varying fabrics of sea ice.

5 Discussion

In the discussion section possible sources of uncertainty in the experimental measurements compared to the calculated values will be discussed as well as the realism of the laboratory sea ice and potential limitations of the sea ice simulator.

5.1 Sources of uncertainty in the experimental measurements compared to the calculated values

The comparison between experimentally measured and calculated values reported here are presented under the assumption that the experimental conditions are accurately replicated by the TUV-snow radiative-transfer model. Potential sources for uncertainty in comparing experimentally measured values to calculated values include: aggregation of black carbon particles; mobilization of black carbon from the top layer of sea ice into the underlying ice and sea water; the value of the asymmetry parameter used in the radiative-transfer modelling; uncertainty in the derived scattering and absorption cross sections of the experimental sea ice; and uncertainty in the mass ratio of black carbon added to the laboratory sea ice. The possible contribution of each of these factors is subsequently reviewed.

5.1.1 Aggregation of particles

The effect of aggregation of black carbon particles decreases the absorption cross section in two ways. Assuming that two black carbon particles aggregate to form a new spherical black carbon particle, the newly formed particle would have twice the volume and the radius would be a factor of $\sqrt[3]{2}$ larger. Mie calculations show that the absorption cross section would decrease and the mass-absorption cross section would decrease and flatten according to Dang et al. (2015). Secondly, aggregation would reduce the number density of black carbon particles, further reducing the absorption of light within the ice. However, the good agreement shown between measured and calculated reflectance for the black-carbon-doped ice suggests that aggregation is not occurring within the ice.

5.1.2 Black carbon mobilization

The radiative-transfer model assumes that the black carbon is distributed evenly within the black-carbon-doped layer. However, the experimental ice may not have had an even distribution. Sea ice forms brine pockets and brine channels on freezing (e.g. Weeks, 2010). As the extra layer of seawater freezes, brine will drain downwards into the layer of ice below and also be expelled onto the surface. Eicken (2003) suggest that impurities in seawater are trapped in the brine inclusions as sea ice grows. If black carbon is situated in brine inclusions, then some of it may drain into the underlying layer of sea ice and eventually into the underlying seawater, as described by Eicken (2003). Doherty et al. (2010), who measured black carbon mass ratios in sea ice in the Arctic, showed that black carbon is concentrated at the surface of the sea ice but also found in smaller concentrations throughout the ice, supporting the idea that black carbon deposited onto the surface of sea ice can be mobilized through the ice. If there was a reduced black carbon mass ratio in the upper
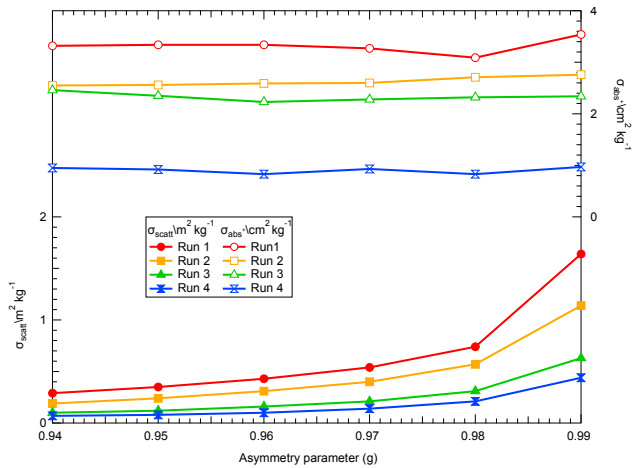
Figure 11. Variation in absorption cross section σ_{abs}^{+} ($cm^2 kg^{-1}$; upper, non-filled markers) and scattering cross section σ_{scatt} ($m^2 kg^{-1}$; lower, filled symbols) owing to variation in the asymmetry parameter at 400 nm. Note that the scatter in the values of σ_{abs}^{+} is due to the fitting process used.

layer then surface reflectance would increase (e.g. Marks and King, 2013).

5.1.3 Asymmetry parameter

A value of the asymmetry parameter, g, of 0.95 was used based on the work of Mobley et al. (1998). However, Mobley et al. (1998) demonstrate that g may vary between 0.94 and 0.99. Figure 11 shows the effect on the determination of the absorption cross section σ_{abs}, owing to absorption by impurities and the ice scattering cross section at 400 nm, for changing the value of g within possible values for sea ice: 0.94–0.99 (Mobley et al., 1998).

The change in the g value has very little effect on the values of absorption cross section, as also noted by Libois et al. (2013), with variation in g between 0.94 and 0.99 having only a factor of 0.092 effect on the absorption cross section, demonstrating the model is insensitive to the value of g for determining light-absorbing impurities.

In the case of scattering cross section, the effect of changing g from 0.94 to 0.99 at 400 nm has a much larger effect on the scattering cross section, with a larger g value giving a larger scattering cross section – i.e. the similarity principle. An increase in the scattering cross section would change the shape of the reflectance–wavelength curve as well as the values of reflectance, as absorbing impurities have less effect in a sea ice with a large scattering cross section compared to a small one, as described in Marks and King (2014).

5.1.4 Uncertainty in derived scattering and absorption cross section and black carbon mass ratio

The determination of the cross section for light scattering and absorption, described in Sect. 4.2.2, depends on varying their values to reproduce the measured values of the e-folding depth and the nadir reflectivity within the experimental uncertainties of measured values of the e-folding depth and the nadir reflectivity, all as a function of wavelength. The latter assists in constraining the determination of the values of the cross section for absorption and scattering. The propagated uncertainty in the determined values of the cross sections for light scattering and absorption from uncertainties in either the value of the e-folding depth or nadir reflectivity in isolation have not been calculated, as our method fits both e-folding depth and reflectivity. Considering the experimental uncertainty in e-folding depth and nadir reflectivity gives a more representative uncertainty of the process. The uncertainty in the reflectance and e-folding depth measurement data of the undoped ice is shown in Figs. 7 and 8. Table 1 gives an indication of the uncertainty in the derived scattering cross section, which is estimated by varying the values of σ_{scatt} and σ_{abs} and still obtaining a good fit (by eye) to the experimental data within the uncertainties of the measured e-folding depth and nadir reflectivity.

5.2 Realism of artificial sea ice

The sea ice simulator is designed to replicate natural sea ice growth in a controlled environment. Section 5.2 will review how the measured physical and optical parameters of the sea ice compare to field measurements of sea ice to ascertain how the laboratory sea ice compares to natural ice. Although the simulator creates a realistic sea ice environment, as with all simulators there are limitations in the degree to which a "natural" sea ice environment can be created. Limitations in the following metrics were noted; light intensity, uneven ice growth, hyper-saline seawater, surface brine expulsion and reflectance measurements.

Temperature profiles from the laboratory sea ice show a linear increase in temperature from the surface to the ice base; this has been commonly reported (e.g. Eicken, 2003; Perovich et al., 1998). Eicken (2003) suggested that at typical winter temperatures ice would take ∼ 1 month to form 50 cm; this is a similar growth rate to that observed for the laboratory-grown sea ice, where it took approximately 3 weeks to grow 30 cm of ice.

Typical sea ice densities are reviewed by Timco and Frederking (1996) reporting first-year sea ice densities in the range 0.84 to 0.94 $g\,cm^{-3}$. The density of sea ice created in the simulator ranged from 0.85 to 0.95 $g\,cm^{-3}$, thus being in the range of natural ice. Perovich et al. (1998) measured density profiles through Arctic first-year sea ice showing no clear variation with depth, which is also observed in the laboratory sea ice.

Plots of salinity versus depth from ice cores from the sea ice simulator show the distinctive "C" shape, with a higher salinity seen at the base and top of the cores – see Fig. 6. Malgrem et al. (1927) studied salinity of first-year ice and also found a characteristic "C" shape to the sea ice salinity profile. The shape of the salinity profile, explained by Eicken (2003), is due to a combination of salt segregation, gravity drainage and brine expulsion on the surface of the ice. Initially, as sea ice in the simulator grows, the seawater below the ice increases in salinity and, similarly to natural sea ice, the seawater below the ice is commonly hyper-saline. As the simulator continues to generate thicker sea ice there is an increase in the salinity of the brine beneath the sea ice which may eventually retard the growth and the water might become unrealistically saline if the experiment were to be allowed to continue. In the experiment discussed here this is not a major problem, as the experiments were performed with ice thicknesses of 30 cm.

The typical structure of a first-year sea ice is described by Eicken (2003) showing a granular surface layer, overlying columnar ice with granular/platelet ice at the ice–water boundary. The structure described by Eicken (2003) is the same as that observed in ice cores of the laboratory-grown ice. The surface of the laboratory-grown ice has a clear granular texture, and at the base there is a slushy platelet layer, with columnar ice in between.

Although the sides of the tank are insulated, ice growth across the tank is not quite uniform, with slightly thicker ice (~ 5 cm) around the edges of the tank towards the end of an experiment (~ 3 cm from the sides) and around the polypropylene pole which the thermocouples were inserted into. Unfortunately, the thicker ice areas could not be rectified, but this was unimportant as reflectance measurements were taken in the same place, away from the sides of the tank. All measurements of the extinction coefficient/e-folding depth were made more than three e-folding depths from the sides of the tank so that any extra ice growth at the edges of the tank would have no impact on the measurements.

Typical extinction coefficients of sea ice at around 500 nm are around ~ 0.03 cm^{-1} (Grenfell and Maykut, 1977). Calculated extinction coefficients for the laboratory-grown ice range from 0.1 to 0.03 cm^{-1}.

Overall, the sea ice simulator creates a realistic sea ice, recreating typical growth rates, salinity and temperature profiles, and reflectance and extinction coefficients of a first-year sea ice.

6   Conclusions

The study has shown that the TUV-snow radiative-transfer model can reproduce reflectivity of undoped and black-carbon-doped sea ice with different sea ice fabrics, and thus the model can be used with confidence. Black carbon in labo-

ratory sea ice has been shown to reduce the reflectivity of the ice to 97, 90 and 79 % of the clean ice reflectivity at a wavelength of 500 nm for mass ratios of 75, 150 and 300 ng g^{-1} of black carbon respectively in the top 5 cm layer of the laboratory sea ice, which is in agreement with radiative-transfer calculations. To reproduce the reflectivity using the TUV-snow model, measured reflectivity and e-folding depth data from laboratory sea ice were used to derive scattering and absorption cross sections of the ice using the TUV-snow model. The derived scattering cross section values are typical of sea ice (e.g. Grenfell and Maykut, 1977; Timco and Frederking, 1996; Perovich, 1996), while the derived absorption cross sections show the presence of other absorbing impurities in the undoped ice, which match the absorption spectra of algae.

The Supplement related to this article is available online at https://doi.org/10.5194/tc-11-2867-2017-supplement.

References

Abramoff, M., Magalhaes, P., and Ram, S.: Image Processing with ImageJ, Biophotonics Int., 11, 36–42, 2004.

Atkinson, M. and Bingman, C.: Elemental composition of commercial seasalts, J. Aquariculture Aquatic Sci., 8, 39–43, 1997.

Ball, C., Levick, A., Woolliams, E., Green, P., Dury, M., Winkler, R., Deadman, A., Fox, N., and King, M.: Effect of polytetrafluoroethylene (PTFE) phase transition at 19 °C on the use of Spectralon as a reference standard for reflectance, Appl. Optics, 52, 4806–4812, 2013.

Bond, T., Doherty, S., Fahey, D., Forster, P., Berntsen, T., DeAngelo, B., Flanner, M., Ghan, S., Kärcher, B., and Koch, D.: Bounding the role of black carbon in the climate system: A scientific assessment, J. Geophys. Res.-Atmos., 118, 5380–5552, 2013.

Boyer, T. P., Antonov, J. I., Baranova, O. K., Coleman, C., Garcia, H. E., Grodsky, A., Johnson, D. R., Locarnini, R. A., Mishonov, A. V., O'Brien, T. D., Paver, C. R., Reagan, J. R., Seidov,

D., Smolyar, I. V., Zweng, M. M.: World Ocean Database 2013, Sydney Levitus, edited by: Alexey, M., NOAA Atlas NESDIS 72, 209 pp., https://doi.org/10.7289/V5NZ85MT, 2013.

Brandt, R. E., Warren, S. G., and Clarke, A. D.: A controlled snow-making experiment testing the relation between black carbon content and reduction of snow albedo, J. Geophys. Res.-Atmos., 116, D08109, https://doi.org/10.1029/2010JD015330, 2011.

Bricaud, A., Claustre, H., Ras, J., and Oubelkheir, K.: Natural variability of phytoplanktonic absorption in oceanic waters: Influence of the size structure of algal populations, J. Geophys. Res., 109, C11010, https://doi.org/10.1029/2004JC002419, 2004.

Buist, I., Potter, S., Nedwed, T., and Mullin, J.: Herding surfactants to contract and thicken oil spills in pack ice for in situ burning, Cold Reg. Sci. Technol., 67, 3–23, https://doi.org/10.1016/j.coldregions.2011.02.004, 2011.

Clarke, A.: Integrating sandwich: a new method of measurement of the light absorption coefficient for atmospheric particles, Appl. Optics, 21, 3011–3020, https://doi.org/10.1364/AO.21.003011, 1982.

Clarke, A. and Noone, K.: Soot in the Arctic snowpack: A cause for perturbations in radiative transfer, Atmos. Environ., 19, 2045–2053, 1985.

Dang, C., Brandt, R. E., and Warren, S. G.: Parameterizations for narrowband and broadband albedo of pure snow and snow containing mineral dust and black carbon., J. Geophys. Res.-Atmos., 120, 5446–5468, 2015.

Doherty, S. J., Warren, S. G., Grenfell, T. C., Clarke, A. D., and Brandt, R. E.: Light-absorbing impurities in Arctic snow, Atmos. Chem. Phys., 10, 11647–11680, https://doi.org/10.5194/acp-10-11647-2010, 2010.

Eicken, H.: Sea ice-an introduction to its physics, biology, chemistry and geology, chap. From the microscopic, to the macroscopic, to the regional scale: growth, microstructure and properties of sea ice, Blackwell Science, London, 2003.

Flanner, M., Zender, C., Randerson, J., and Rasch, P.: Present-day climate forcing and response from black carbon in snow, J. Geophys. Res., 112, D11202, https://doi.org/10.1029/2006JD008003, 2007.

France, J. and King, M.: The effect of measurement geometry on recording solar radiation attenuation in snowpack (e-folding depth) using fibre-optic probes, J. Glaciol., 58, 417–418, https://doi.org/10.3189/2012JoG11J227, 2012.

France, J. L., King, M. D., Frey, M. M., Erbland, J., Picard, G., Preunkert, S., MacArthur, A., and Savarino, J.: Snow optical properties at Dome C (Concordia), Antarctica; implications for snow emissions and snow chemistry of reactive nitrogen, Atmos. Chem. Phys., 11, 9787–9801, https://doi.org/10.5194/acp-11-9787-2011, 2011.

France, J., Reay, H., King, M., Voison, D., Jacobi, H., Domine, F., Beine, H., Anastasio, C., MacArthur, A., and Lee-Taylor, J.: Hydroxyl Radical and NO_x producion rates, black carbon concentrations and light-absorbing impurities in the snow from field measurements of light penetration and nadir reflectivity of on-shore and off-shore coastal Alaskan snow, J. Geophys. Res., 117, D00R12, https://doi.org/10.1029/2011JD016639, 2012.

Goldenson, N., Doherty, S. J., Bitz, C. M., Holland, M. M., Light, B., and Conley, A. J.: Arctic climate response to forcing from light-absorbing particles in snow and sea ice in CESM, At-

mos. Chem. Phys., 12, 7903–7920, https://doi.org/10.5194/acp-12-7903-2012, 2012.

Grenfell, T. and Maykut, G.: The optical properties of ice and snow in the Arctic Basin, J. Glaciol., 18, 445–463, https://doi.org/10.1017/S0022143000021122, 1977.

Grenfell, T. and Perovich, D.: Radiation absorption coefficients of polycrystalline ice from 400–1400 nm, J. Geophys. Res., 86, 7447–7450, 1981.

Grenfell, T., Light, B., and Sturm, M.: Spatial distribution and radiative effects of soot in the snow and sea ice during the SHEBA experiment: The surface heat budget of Arctic ocen (SHEBA), J. Geophys. Res., 107, C10, https://doi.org/10.1029/2000JC000414, 2002.

Grenfell, T., Doherty, S., Clarke, A., and Warren, S.: Light absorption from particulate impurities in snow and ice determined by spectrophotometric analysis of filters, Appl. Optics, 50, 2037–2048, 2011.

Haas, C., Cottier, F., Smedsrud, L., and Thomas, D.: Multidisciplinary ice tank study shedding new light on sea ice growth processes, EOS, Transactions, 80, 507–513, 1999.

Hadley, O. and Kirchstetter, T.: Black carbon reduction of snow albedo, Nature Clim. Change, 2, 437–440, 2012.

Hansen, J. and Nazarenko, L.: Soot climate forcing via snow and ice albedos, P. Natl. Acad. Sci. USA, 101, 423, https://doi.org/10.1073/pnas.2237157100, 2004.

Hare, A., Wang, F., Barber, D., Geilfus, N., and Galley, R.: pH evolution in sea ice grown at an outdoor experimental facility, Marine Chem., 154, 46–54, https://doi.org/10.1016/j.marchem.2013.04.007, 2013.

Heilbronner, R. and Barrett, S.: Image analysis in Earth Sciences: microstructures and textures of earth materials, Springer Science and Business Media, 129, 520 pp., 2013.

Highwood, E. and Kinnersley, R.: When smoke gets in our eyes: The multiple impacts of atmospheric black carbon on climate, air quality and health, Environ. Int., 32, 560–566, 2006.

Holland, M., Bailey, D., Breigleb, B., Light, B., and Hunke, E.: Improved sea ice short wave radiation physics in CCSM4: The impact of melt ponds and aerosols on Arctic sea ice, J. Climate, 25, 1413–1430, 2012.

IPCC: IPCC Working Group 1 Fifth Assessment Report Summary for Policy Makers - Climate Change 2013: The Physical Science Basis., Tech. rep., IPCC, 2013.

Jacobson, M.: Strong radiative heating due to the mixing state of black carbon in atmospheric aerosols, Nature, 409, 695–697, 2001.

Jacobson, M.: Climate response of fossil fuel and biofuel soot, accounting for soot's feedback to snow and sea ice albedo and emissivity, J. Geophys. Res., 109, D21201, https://doi.org/10.1029/2004JD004945, 2004.

Johnston, M. and Timco, G.: Temperature Changes in First Year Arctic Sea Ice During the Decay Process., in: Proceedings of the 16th IAHR International Symposium on Ice, 2, 194–202, 2002.

King, M., France, J., Fisher, F., and Beine, H.: Measurement and modelling of UV radiation penetration and photolysis rates of nitrate and hydrogen peroxide in Antarctic sea ice: An estimate of the production rate of hydroxyl radicals in first-year sea ice, J. Photoch. Photobio. A, 176, 39–49, 2005.

Krembs, C., Mock, T., and Gradinger, R.: A mesocosm study of physical-biological interactions in artificial sea ice: effects of

brine channel surface evolution and brine movement on algal biomass, Polar Biology, 24, 356–364, 2001.

Lamare, M. L., Lee-Taylor, J., and King, M. D.: The impact of atmospheric mineral aerosol deposition on the albedo of snow & sea ice: are snow and sea ice optical properties more important than mineral aerosol optical properties?, Atmos. Chem. Phys., 16, 843–860, https://doi.org/10.5194/acp-16-843-2016, 2016.

Ledley, T. and Thompson, S.: Potential effect of nuclear war smoke-fall on sea ice, Clim. Change, 8, 155–171, 1986.

Lee-Taylor, J. and Madronich, S.: Calculation of actinic fluxes with a coupled atmosphere-snow radiative transfer model, J. Geophys. Res., 107, 4796, https://doi.org/10.1029/2002JD002084, 2002.

Libois, Q., Picard, G., France, J. L., Arnaud, L., Dumont, M., Carmagnola, C. M., and King, M. D.: Influence of grain shape on light penetration in snow, The Cryosphere, 7, 1803–1818, https://doi.org/10.5194/tc-7-1803-2013, 2013.

Light, B., Eicken, H., Maykut, G., and Grenfell, T.: The effect of included particulates on the spectral albedo of sea ice, J. Geophys. Res., 103, 27739–27752, 1998.

Light, B., Carns, R., and Warren, S.: "Albedo dome": A method for measuring spectral flux-reflectance in a laboratory for media with long optical paths, Appl. Optics, 54, 5260–5269, 2015.

Malgrem, F., Institutt, G., Forskningsfond, S., and Fond, N.: The Norwegian Polar Expedition 'Maud,' 1918–1925: Scientific Results, vol. 1, chap. On the properties of sea-ice, Gofys. Inst., Bergen, Norway, 1–67, 1927.

Marks, A. A. and King, M. D.: The effects of additional black carbon on the albedo of Arctic sea ice: variation with sea ice type and snow cover, The Cryosphere, 7, 1193–1204, https://doi.org/10.5194/tc-7-1193-2013, 2013.

Marks, A. A. and King, M. D.: The effect of snow/sea ice type on the response of albedo and light penetration depth (e-folding depth) to increasing black carbon, The Cryosphere, 8, 1625–1638, https://doi.org/10.5194/tc-8-1625-2014, 2014.

Marks, A., Lamare, M., and King, M.: Data for "Optical properties of sea ice doped with black carbon – an experimental and radiative-transfer modelling comparison", available at: https://doi.org/10.5281/zenodo.1067150, 2017.

Mitchell, J.: Visual range in the polar regions with particular reference to the Alaskan Arctic, J. Atmos. Terr. Phys. Special Supplement, 195–211, 1957.

Mobley, C., Cota, G., Grenfell, T., Maffione, R., Pegau, W., and Perovich, D.: Modeling light propagation in sea ice, Geoscience and Remote Sensing, IEEE Transactions on, 36, 1743–1749, 1998.

Mock, T., Dieckmann, G., Haas, C., Krell, A., Tison, J., Belem, A., Papadimitriou, S., and Thomas, D.: Micro-optodes in sea ice: a new approach to investigate oxygen dynamics during sea ice formation, Aquat. Microb. Ecol., 29, 297–306, https://doi.org/10.3354/ame029297, 2002.

Mundy, C., Gosselin, M., Ehn, J., Belzile, C., Poulin, M., Alou, E., Roy, S., Hop, H., Lessard, S., Papakyriakau, T., Barber, D., and Stewart, J.: Characteristics of two distinct high-light acclimated algal communities during advanced stages of sea ice melt, Polar Biology, 34, 1869–1886, 2011.

Nomurai, D., Yoshikawa-Inoue, H., and Toyota, T.: The effect of sea-ice growth on air–sea CO_2 flux in a tank experiment, Tellus B, 58, 2006.

Papadimitriou, S., Kennedy, H., Kattner, G., Dieckmann, G., and Thomas, D.: Experimental evidence for carbonate precipitation and CO_2 degassing during sea ice formation, Geochem. Cosmochim. Ac., 68, 1749–1761, 2003.

Peltoniemi, J. I., Gritsevich, M., Hakala, T., Dagsson-Waldhauserová, P., Arnalds, Ø., Anttila, K., Hannula, H.-R., Kivekäs, N., Lihavainen, H., Meinander, O., Svensson, J., Virkkula, A., and de Leeuw, G.: Soot on Snow experiment: bidirectional reflectance factor measurements of contaminated snow, The Cryosphere, 9, 2323–2337, https://doi.org/10.5194/tc-9-2323-2015, 2015.

Perovich, D.: The Optical Properties of Sea Ice., US Army Corps of Engineers: Cold Regions Research and Engineering Laboratory, 96, 1996.

Perovich, D. and Grenfell, T.: Laboratory studies of the optical properties of young sea ice, J. Glaciol., 27, 331–346, https://doi.org/10.1017/S0022143000015410, 1981.

Perovich, D., Roesler, C., and Pegau, W.: Variability in Arctic sea ice optical properties, J. Geophys. Res., 103, 1193–1208, 1998.

Phillips, G. and Simpson, W.: Verification of snowpack radiation transfer models using actinometry, J. Geophys. Res., 110, D08306, https://doi.org/10.1029/2004JD005552, 2005.

Polach, R., Ehlers, S., and Kujala, P.: Model-Scale Ice-Part A: Experiments, Cold Reg. Sci. Technol., 94, 74–81, 2013.

Rabus, B. and Echelmeyer, K.: Increase of 10 m ice temperature: climate warming or glacier thinning?, J. Glaciol., 48, 279–286, https://doi.org/10.3189/172756502781831430, 2002.

Ramanathan, V. and Carmichael, G.: Global and regional climate changes due to black carbon, Nature Geosci., 1, 221–227, 2008.

Rand, J. and Mellor, M.: Ice-coring augers for shallow depth sampling, Tech. Rep. 85-21, CRREL, Washington, 1985.

Reay, H., France, J., and King, M.: Decreased albedo, efolding depth and photolytic OH radical and NO_2 production with increasing black carbon content in Arctic snow., J. Geophys. Res., 117, D00R20, https://doi.org/10.1029/2011JD016630, 2012.

Stamnes, K., Tsay, S., Jayaweera, K., and Wiscombe, W.: Numerically stable algorithm for discrete-ordinate-method radiative transfer in multiple scattering and emitting layered media, Appl. Optics, 27, 2502–2509, 1988.

Timco, G. and Frederking, R.: A review of sea ice density, Cold Reg. Sci. Technol., 24, 1–6, 1996.

Weeks, W.: On sea ice, chap. Snow, pp. 417–433, University of Alaska Press, 2010.